

## RESEARCH ARTICLE

# Power Quality Management Using FACTS Device for Grid-Connected PV Solar and Wind Turbine Systems

John Abban<sup>ORCID</sup>, Patrick Ayambire<sup>ORCID</sup>, Francois Sekyere<sup>ORCID</sup>, Albert Awopone<sup>ORCID</sup>

Department of Electrical and Electronic Engineering, Akenten Appiah-Menka University of Skills Training and Entrepreneurial Development (AAMUSTED), Kumasi, Ghana

**Cite this article as:** J. Abban, P. Ayambire, F. Sekyere and A. Awopone, "Power management using FACTS device for grid-connected PV solar and wind turbine systems," *Turk J Electr Power Energy Syst.*, 2025; 5(1), 54-65.

## ABSTRACT

This study investigates the use of Flexible AC Transmission System (FACTS) devices for power quality management in grid-connected photovoltaic (PV) solar and wind turbine systems within the GA West Municipal District electricity grid in Accra. With a growing reliance on renewable energy sources for sustainable solutions, understanding their impact on low-voltage (LV) networks and effective management strategies is crucial. The study aims to assess the effects of hybrid PV and wind systems, modeling and simulating the GA West Network and IEEE-Low-Voltage Distribution Network (LVDN) and focusing on power factor, active, and reactive power. A 19-busbar test network was modeled to evaluate PV and wind turbine integration with the grid, and IEEE-LVDN was used for validation. The study employed the MATLAB/Simulink simulations. Results show that FACTS devices substantially improve power factor, achieve near-unity levels, and enhance overall network performance by reducing active and reactive power losses. The analysis confirms that FACTS devices boost system capacity, stability, and dynamic behavior. The findings indicate that integrating FACTS devices in grid-connected renewable systems effectively manages power quality and optimizes network performance.

**Index Terms**—Low-voltage distribution, network, power factor, power quality management, solar PV

## I. INTRODUCTION

Grid-connected photovoltaic (PV) solar and wind turbine (WT) systems are becoming increasingly popular as renewable energy sources (RES). However, these systems can host power quality issues, such as voltage fluctuations, harmonics, and unbalanced loads, which may negatively affect the grid's performance [1]. Power quality management strategies are needed to address these issues, and flexible AC transmission systems (FACTS) devices have been developed as effective solutions. Many experts in the field are trying to discover an alternative solution as a substitute energy source. Renewable sources such as solar, wind, and biomass are economically viable sources and pollution-free solutions for providing green energy to many loads. [2, 3]. Solar and wind sources according to experts are the best providers of present-day energy sources, yet, solar sources remain outstanding among all renewables due to their accessibility and promising nature for various power [2]. The study aims to investigate the impact of grid-connected PV solar and WT systems on the power quality of low-voltage (LV) networks by modeling and

simulating the GA West local grid and validating with a modified IEEE-Low-Voltage Distribution Network (LVDN).

## II. RELATED WORKS

Power quality management is critical for ensuring the reliable and efficient operation of LVDNs, especially in the context of increasing Distributed Energy Resources (DERs) [4]. The study has chosen GA West Network as a case study. The IEEE European LVDN is a standardized test system extensively employed in research and analysis integration of DERs. Numerous studies have leveraged the IEEE European LVDN to explore the integration of renewable energy sources, such as solar PVs and wind power. One significant area of research has been the impact of high penetration levels of DERs on voltage profiles and network stability [5]. For instance, studies have [6, 7] investigated voltage regulation challenges in LVDNs with substantial PV integration, highlighting the need for advanced voltage control strategies. Similarly, Majeed and Nwulu [8] examined the effects of wind power integration on

**Corresponding author:** John Abban, abbanjohn34@gmail.com



Content of this journal is licensed under a Creative Commons Attribution (CC BY) 4.0 International License.

**Received:** October 2, 2024  
**Revision requested:** October 25, 2021  
**Last revision received:** November 1, 2024  
**Accepted:** November 17, 2024  
**Publication Date:** January 13, 2025

the network and proposed methods to mitigate adverse impacts on power quality. The accurate representation of consumer load profiles is crucial for realistic simulations of LVDNs. Studies such as those by Abban and Awoopone [9] have utilized the IEEE European LVDN to model residential load patterns and assess the potential of demand response programs. Their findings indicate that demand response can significantly enhance grid flexibility and support the integration of intermittent renewable energy sources. Maintaining grid stability in high DER penetration is a critical challenge addressed in the literature. Research by Gandhi and Sampath [10] focused on the impact of reverse power flow on distributed transformers in a PV solar configuration of LV networks, including dynamic voltage control, to maintain stability in LVDNs. The power consumption and demand management operations of the Municipal District Network and its associated equipment require a significant amount of electricity. Proper demand management and energy-efficient practices are essential to considering the energy scenarios in Ghana [9].

The power factor (PF) measures the efficiency of power between the grid and the load. A low PF can lead to increased power losses and reduced efficiency in electrical equipment. Renewable energy sources, such as PV solar and wind turbine systems, can lead to a low PF due to the reactive power generated by these sources [10]. Power factor control is, therefore, necessary to maintain [11]. A high power factor ensures efficient power flow. For instance, studies [6, 12] have investigated the use of static synchronous compensators (STATCOM) for improving the power quality of a grid-connected PV solar system. The outcome showed that STATCOM effectively regulated the voltage and reduced the harmonic bias in the system, thereby improving frequency. FACTS device, the STATCOM per its design is connected at a point of coupling with a battery storage system to moderate power quality [13]. With the incorporation of wind generation and FACTS devices with a battery storage scheme, the grid-connected system achieves power quality standards by the IEC standard 61400-2, as presented in the Fig. 1 [14].

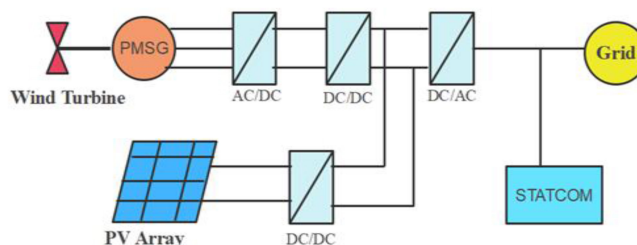


**Fig. 1.** Hybrid solar PV and wind turbine with STATCOM connected to grid.

Benali et al. [7] proposed a FACTS device, SVC light, to be linked at a Point of Common Coupling. This strategy was provided for the wind energy source integration to improve power quality. Grid-connected PV solar and wind turbine systems generate electricity from the sun and the wind [15]. The utility grid can provide excess power when the renewable energy source is producing more than the system needs, and it can also draw electricity from the grid when the renewable energy source is less than what the system needs [16]. Grid-connected PV solar systems convert sunlight into electricity using PV cells, according to ref. [17]. The power output of the PV array is dependent on the solar irradiance and temperature [18]. Wind turbine systems generate electricity from wind energy using a rotor that is connected to a generator. The output power of a wind turbine is dependent on the wind speed and direction [19].

### III. METHODOLOGY

The study employed MATLAB Simulink simulation for the models to compare and analyze their differences. The modules consist of the following models: 1) the GA West Network as a case study; 2) the GA West Network connected with a FACTS device; and 3) the model of the IEEE LVDN.

### IV. CASE STUDY NETWORK

This study focuses on the GA West Municipal District network in the Greater Accra region of Ghana, examining its radial LV distribution grid configuration. The network is linked to the medium voltage grid through a three-phase, four-wire system equipped with 11/0.415 kV transformers, and an interconnected 200 kVA transformer, as depicted in Fig. 2. The network faces occasional power outages and discrimination issues, prompting the proposed integration of solar PV and wind turbine power to enhance the voltage profile. To assess the peak load on the 11 kV feeder, data from an Electricity Company of Ghana (ECG) in 2023 concerning the distribution transformer were utilized. The recorded load current indicated a peak current of 255 A. Determining the transformer's overall maximum operational load follows the outlined procedure, considering the identified challenges in the existing network. Hence, the transformer's rated kVA at full load is 183.29 kVA for the solar PV rating.

$$\text{Case Study Transformer Rating} = \frac{\sqrt{3} \times V_L I_L}{1000} = \frac{\sqrt{3} \times 255 \times 415}{1000} \quad (1)$$

To model the GA West Network and test it using a modified LVDN system, a power flow analysis was set up to calculate reactive power, active power, PF voltage, and current. This model

#### Main Points

- The study examines the use of flexible AC transmission system (FACTS) devices, particularly static synchronous compensators (STATCOM), for managing power quality in a grid that connects photovoltaic solar and wind turbine systems in the GW West municipal district of Accra.
- The study modeled and analyzed the GA West Network and IEEE low-voltage distribution network, comparing the performance of FACTS devices regarding power factor, active, and reactive power.
- The results demonstrated that FACTS devices significantly improve the power factor, bringing it close to unity, and enhancing overall network performance by reducing active and reactive power losses.
- This confirms that FACTS devices improve system stability, capacity, and dynamic behavior, making them effective tools for optimizing power quality and network performance in grid-connected renewable energy systems.

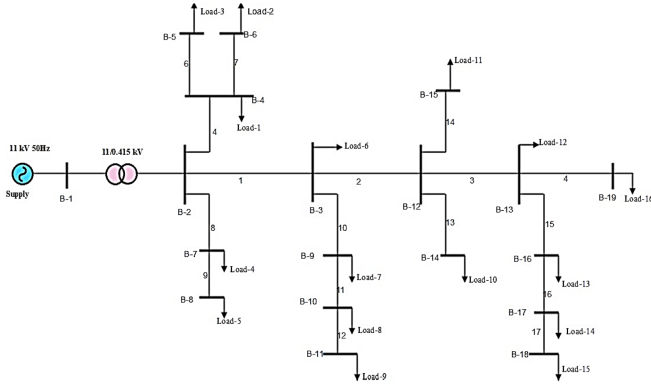


Fig. 2. Single line diagram of GA West Network.

was used to determine the steady-state operating conditions of the combined system. Below are the equations and calculations for each of these parameters: the active and reactive power at each bus can be calculated using the following equations in (2) and (3):

Active power ( $P$ ):

$$P_s = V_s \sum_{j=1}^n V_s \cdot [G_j \cdot \cos(\theta_1 - \theta_2) + B_j \cdot \sin(\theta_1 - \theta_2)] \quad (2)$$

Reactive power ( $Q$ ):

$$Q_s = V_s \sum_{j=1}^n V_s \cdot [G_j \cdot \sin(\theta_1 - \theta_2) - B_j \cdot \cos(\theta_1 - \theta_2)] \quad (3)$$

where  $P_s$  = active power at the bus,  $Q_s$  = reactive power at the bus,  $V_s$  = voltage magnitude at the bus,  $n$  = total number of buses,  $G_j$  = real part of the admittance (conductance) between buses,  $B_j$  is the imaginary part of the admittance (susceptance) between buses, and  $\theta_1$  and  $\theta_2$  are the phase angles at buses.

$$Pf = \frac{P_s}{\sqrt{P_s^2 + Q_s^2}} \quad (4)$$

where  $Pf$  is the power factor at the bus.

Current ( $I$ ):

$$I_s = \frac{P_s + jQ_s}{V_s (G + jB)} \quad (5)$$

$Z$  is the purely real, that is, when  $Z = R + j0$ , the admittance  $Y$  is identical to conductance  $Y = G + jB$ .

$$Y = G + jB = \frac{1}{Z} = \frac{1}{R + jX} \quad (6)$$

To express  $Y$  in the form  $Y = G + jB$ , multiply the numerator and denominator by  $R - jX$ ,  $G$ , and  $B$  are related to  $R$  and  $X$ :

$$Y = \frac{1}{R + jX} \frac{R - jX}{R - jX} = \frac{R - jX}{R^2 + X^2} = \frac{R}{R^2 + X^2} - j \frac{X}{R^2 + X^2} \quad (7)$$

where  $I_s$  is the current magnitude on the transmission line between buses,  $Z$  is the impedance of the line,  $R$  is resistance, and  $X$  is the inductance

The description of hybrid solar PV connected to the GA West Network consists of a solar PV power system, and GA West Network to form the spanner shape as presented in Fig. 3. The PV solar system consists of a solar array, that is, Canadian Solar Inc. CS3U-365MS-AG; 32 series modules, eight parallel strings connected to a 1000  $\mu$ F capacitor, and boost converter that involves six insulated-gate bipolar transistors (IGBT). This IGBT is a power transistor that combines an input metal-oxide-semiconductor field-effect transistor technology and an output bipolar transistor as it is a unidirectional device, that is, it can only switch ON forward direction. It has an internal resistance of 0.221  $\Omega$ , a snubbed resistance of 415.405  $\Omega$ , and a snubbed capacitance of infinity. It also modeled a subsystem inverter with six diodes, which is connected to the modeled subsystem of an LC filter. The modeling of the wind power system consists of a transformer, transmission line, and wind turbine induction generator that implements a model of a squirrel-cage induction generator driven by a wind turbine. All components are connected to a common bus at the point of the typical coupling, as presented in Fig. 3 below.

#### V. PHOTOVOLTAIC PANEL MODELING

A solar cell is represented by an equivalent circuit, as depicted in Fig. 4. This equivalent circuit includes components such as the photocurrent source ( $I_{ph}$ ), diode ( $D$ ), series resistance ( $R_s$ ), and parallel resistance ( $R_{sh}$ ). The design of a PV array is grounded in this equivalent circuit. Equation (8) is derived by applying Kirchhoff's current law to the circuit diagram in Fig. 4.

$$I_{pV} = I_{ph} - I_D - I_{sh} \quad (8)$$

In the context of the given parameters:  $I_{pV}$  represents the current of the PV module in amperes (A),  $I_{ph}$  denotes the current due to incident light or photocurrent in amperes (A),  $I_D$  signifies the current flowing through the diode of the PV module in amperes (A), and  $I_{sh}$  is indicative of the current through the parallel resistance of the PV module in amperes (A).

$$V_D = V_{pV} + I_{pV} R_s \quad (9)$$

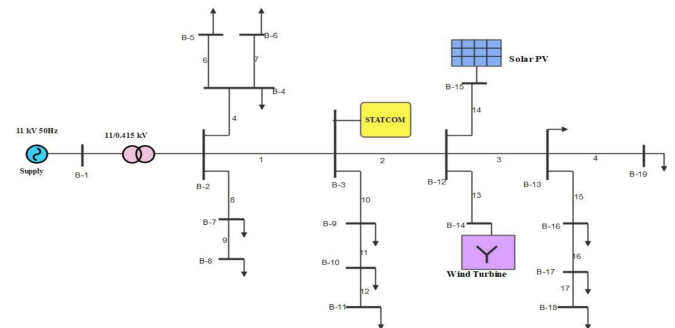


Fig. 3. GA West Network GA West Network connected to hybrid solar PV and wind turbine with STATCOM.

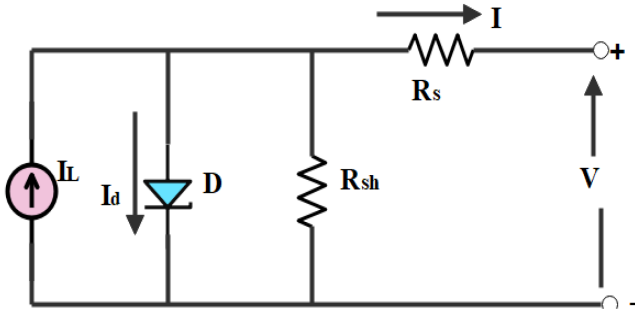


Fig. 4. Equivalent circuit of PV solar cell.

In the given context:  $V_D$  represents the voltage across the diode of the PV module in volts (V),  $V_{pv}$  stands for the PV module current in amperes (A), and  $R_s$  signifies the PV module series resistance in ohms ( $\Omega$ ). The expression for shunt current ( $I_{sh}$ ) flowing through the parallel resistance ( $R_{sh}$ ) is derived in (10) by applying Kirchoff's voltage law to the circuit diagram in Fig. 4.

$$I_{sh} = \frac{V_{pv} + I_{pv} \times R_s}{R_{sh}} = \frac{V_D}{R_{sh}} \quad (10)$$

The thermal voltage can be expressed as (11):

$$V_T = \frac{K \times T}{q \times N_{CELL} \times Q_p} \quad (11)$$

In the given context:  $V_T$  is the thermal voltage in volts,  $K$  is the Boltzmann constant, which is  $1.3806e^{-22} \text{JK}^{-1}$ ,  $T$  represents the cell temperature, set at  $25^\circ\text{C}$ ,  $q$  signifies the electron charge, equal to  $1.6022e^{-19} \text{C}$ ,  $N_{CELL}$  indicates the number of series-connected cells per module, and  $Q_p$  is the diode quality factor of the PV module, specified as 1.25. Here,  $I_{ph}$  represents the photocurrent generated by solar irradiation, as expressed in (12).

$$I_{ph} = I_{sc} + K_i (T_{ak} - T_{rk}) \left[ \frac{G}{G_{ref}} \right] \quad (12)$$

In the provided context:  $I_{sc}$  designates the short circuit current in amperes (A),  $K_i$  represents the temperature coefficient under short circuit conditions,  $T_{ak}$  corresponds to the surface temperature of the PV module in degrees Celsius ( $^\circ\text{C}$ ),  $T_{rk}$  denotes the reference temperature in degrees Celsius ( $^\circ\text{C}$ ),  $G$  signifies the solar irradiation in Watts per square meter ( $\text{W}/\text{m}^2$ ), and  $G_{ref}$  is the reference solar irradiation, expressed in Watts per square meter ( $\text{W}/\text{m}^2$ ). Shockley's diode current  $I_D$  is expressed in (6).

$$I_D = I_{sat} \times \left[ e^{\left( \frac{V_D}{V_T} \right)} - 1 \right] \quad (13)$$

Equations (7) and (11) are substituted into (13), and the PV module current  $I_{pv}$  can be expressed in (14):

$$I_{pv} = I_{ph} - I_s \left[ e^{\left( \frac{q(V_D)}{N_s A_k T_{ak}} \right)} - 1 \right] - \frac{V_D}{R_{sh}} \quad (14)$$

Canadian Solar Inc. CS3U-365MS-AH (the Canadian Solar KuMax CS3U-365MS-AG Datasheet) data are used per Table I to model PV cells. The following equations are considered for measuring the maximum power point conditions for a PV module. The short-circuit current is given by (15):

$$I_{sc} = I_{sc0} \left( \frac{G}{G_{ref}} \right)^\alpha \quad (15)$$

The open-circuit voltage  $V_{oc}$  at any given condition can be expressed by (16):

$$V_{oc} = \left( \frac{T_0}{T} \right)^\gamma \quad (16)$$

The maximum output power of a PV module,  $P_{max}$  is given in (17):

$$P_{max} = \left[ \frac{\left( \frac{V_{oc}}{T_{ak}} \right) - I_L \left( \frac{V_{oc}}{T_{ak}} + 0.72 \right)}{1 + \frac{V_{oc}}{N_s A_k}} \right] \times \left[ 1 - \frac{R_s}{\frac{V_{oc}}{I_{sc}}} \right] \times \left[ \frac{V_{oc0}}{1 + I_{sc0} \left( \frac{G_{ref}}{G} \right)} \right] \cdot \left( \frac{T_0}{T} \right)^\nu \cdot I_{sc0} \left( \frac{G}{G_0} \right)^\alpha \quad (17)$$

TABLE I.  
 SPECIFICATION OF SOLAR PV-PANEL USING CANADIAN SOLAR INC. CS3U-365M AG DATA

Parameter	Rating
Maximum power ( $P_{Max}$ )	365 W
Current at maximum operating point ( $I_{mp}$ )	9.18 A
The voltage at the maximum operating point ( $V_{mp}$ )	39.8 V
Short circuit (SC) current ( $I_{sc}$ )	9.75 A
Open circuit (OC) voltage ( $V_{oc}$ )	47.2 V
Module efficiency	18.4%
Series resistance	0.221
Parallel resistance	415.405
Number of modules connected in a series string ( $N_{sere}$ )	32
Many modules are connected in a parallel string ( $N_{para}$ )	8
Operating temperature	$85^\circ\text{C}$
Cell per module	72
Temperature coefficient of $I_{sc}$	0.017 (%/ $^\circ\text{C}$ )
Temperature coefficient of $V_{oc}$	-0.38039 (%/ $^\circ\text{C}$ )
Solar panel current ( $I_{pv}$ )	8.8179 A
Diode saturation current ( $I_D$ )	$5.5324e^{-10}$ A
Diode ideality factor	1.054

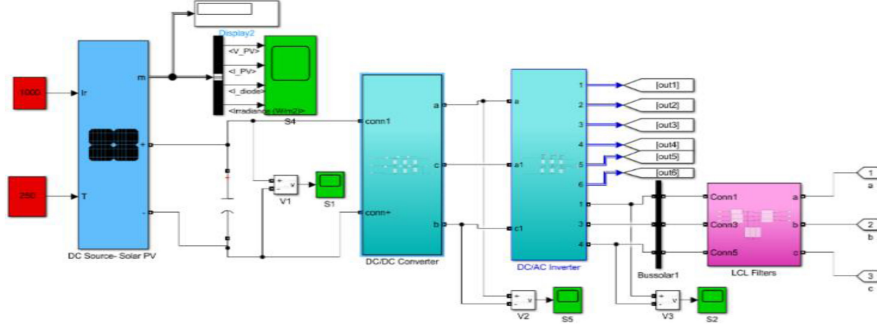


Fig. 5 Solar PV systems.

Fig. 5 presents the solar PV model as a computational tool that simulates the behavior and performance of a solar PV system, aiding in design, optimization, and performance prediction. The components include, PV effect, which converts sunlight into electrical energy. Equivalent Circuit Models, Single-Diode Model, uses a current source, diode, series resistor, and shunt resistor. Double-Diode Model: Adds a second diode for greater accuracy. System Design Parameters: Module specifications (cell configuration, temperature coefficients) and array design (series/parallel connections). Environmental inputs, solar irradiance ( $W/m^2$ ), ambient temperature, and spectral effects, and Performance Curves: Fig. 6 I–V characteristic of PV array at different temperatures and (b) P–V characteristic of PV array at different temperatures. Fig. 7 P-V Curve, highlights the maximum power point (MPP) for optimal efficiency. These models are critical for analyzing PV system performance under varying conditions.

### VI. WIND TURBINE MODELING

Wind power is generated from wind turbines due to the movement of the wind. The energy related to this wind is called kinetic energy. This kinetic energy ( $E$ ) with mass ( $m$ ) and velocity ( $v$ ) can be expressed as (18).

$$Kinetic\ Energy\ (E) = \frac{1}{2}mv^2\ Joule \quad (18)$$

$$m = \text{air mass } (k_g) = \text{air density } \rho\ (k_g/m^3) \times \text{volume } Q\ (m^3)$$

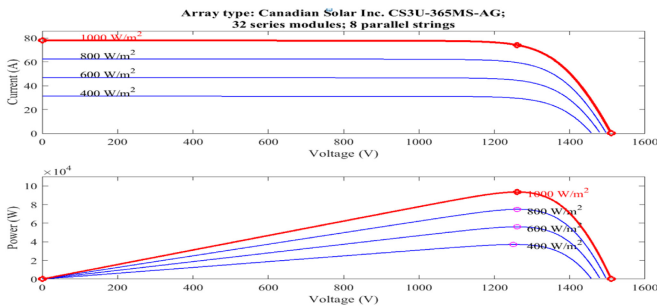


Fig. 6. (a) I–V characteristic of PV array at different temperatures and (b) P–V characteristic of PV array at different temperatures.

$Q$  = discharge.

The expression of power is derived as (19).

$$Power\ (P) = \frac{dE}{dt} = \frac{1}{2} \frac{d}{dt} (mv^2)$$

$$\frac{1}{2} \rho \frac{dQ}{dt} v^2$$

$$Rate\ of\ discharge\ \left(\frac{m^3}{s}\right) = Am^2 \times v\ \left(\frac{m}{s}\right)$$

where  $A$  = swept wind turbine area

$$Power\ (P) = \frac{1}{2} \rho Av^3 \quad (19)$$

The actual power generated by the wind would be smaller due to friction losses. The power coefficient  $C_p$ , defined as a ratio of actual power to theoretical power, can be expressed in (20).

$$C_p = \frac{P_{Actual}}{P_{Theoretical}} \quad (20)$$

Tip speed ratio  $T_{SR}$  is defined as the ratio of the tip speed of the blade divided by wind speed.

It can be expressed as (21):

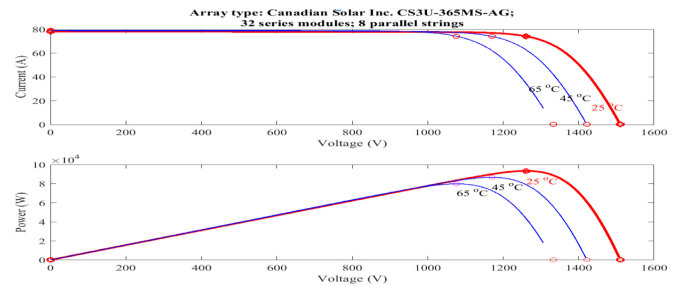


Fig. 7. (a) I–V characteristic of PV array at different temperatures and (b) P–V characteristic of PV array at different temperatures.

**TABLE II.**  
PV SOLAR OUTPUT AT MPPT FOR DIFFERENT IRRADIANCE

Irradiance (W/m <sup>2</sup> )	PV Output		
	V <sub>PV</sub> (V)	I <sub>PV</sub> (A)	P <sub>PV</sub> (W)
400	240.8	8.30	1998.6
600	245.7	16.28	4000
800	246.90	24.30	5999.7
1000	246.2	32.5	8001.5

$$T_{SR} = \frac{\text{Tip Speed of Blade}}{\text{Wind Speed}} = \frac{\omega}{v} \quad (21)$$

Therefore, the amount of power is directly proportional to the area swept out by the rotor, the air density, and the wind speed cube. The amount of power captured by the blade of a wind turbine is expressed as (22).

$$P_m = \frac{1}{2} \rho A C_p \lambda \beta v^3 \quad (22)$$

where  $P_m$  is the mechanical output power,  $C_p$  is the power coefficient,  $\lambda$  is the tip speed ratio,  $\beta$  is the blade angle pitch, and  $\rho$  is the air density. The power coefficient  $C_p$  is a function of  $\beta$ . It can be expressed as (23).

$$C_p = 0.22 \left[ \frac{116}{\beta} - 0.4\theta - 5 \right] e^{-\frac{12.5}{\beta}} \quad (23)$$

## VII. MODELING OF WIND TURBINE PERMANENT MAGNET SYNCHRONOUS GENERATOR

The wind turbine propels the rotor, and the stator winding is directly linked to the grid. Through the induction generator, the wind turbine captures energy and converts it into electrical power, which the stator winding then feeds into the grid. During high wind speeds, the pitch angle is adjusted to limit the generator's output power to its nominal value. For electricity generation, the speed of the induction generator must slightly surpass that of the synchronous generator. However, the wind turbine permanent magnet synchronous generator (WT-PMSG) is commonly classified as a fixed-speed wind generator due to the typically minor speed fluctuations. The grid supplies the reactive power needed by the induction generator, as presented at Fig. 8. The analysis of WT-PMSG model comprises three phases,

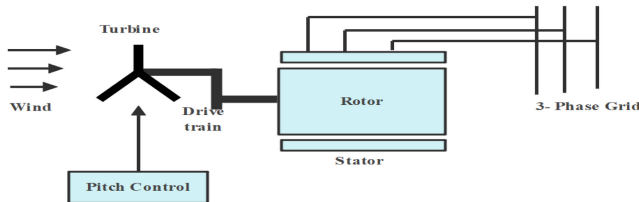


**Fig. 8.** Wind turbine permanent magnet synchronous generator (WT-PMSG).

as illustrated in Fig. 9, which shows the corresponding single-phase circuit of the WT-PMSG. The inclusion of a movable magnetic source and the use of permanent magnets for excitation without additional electrical consumption make the WT-PMSG one of the most efficient all-electric machines. This results in a compact structure for the WT-PMSG, similar to the same-rated induction generator.

Additionally, heat production occurs in the stator, which is easier to cool compared to the rotor, as it is located at the periphery of the generator. Furthermore, the WT-PMSG exhibits a prolonged lifespan for winding insulation, bearings, and magnets, requiring minimal maintenance due to its simplified mechanical design. Moreover, it boasts the highest power-to-weight ratio. These advantages collectively contribute to the widespread utilization of WT-PMSG in wind-integrated systems. This results in a compact structure for the WT-PMSG, similar to the same-rated induction generator. Furthermore, the WT-PMSG exhibits a prolonged life-span for winding insulation, bearings, and magnets, requiring minimal maintenance due to its simplified mechanical design. Moreover, it boasts the highest power-to-weight ratio. These advantages collectively contribute to the widespread utilization of WT-PMSG in wind-integrated systems. The MATLAB Simulink modeling of the WT-PMSG is accomplished using the following equations, with the machine model analyzed in a single phase, as depicted in Fig. 9.

The stator resistance  $R_s$  represents the resistance within the windings of the relatively small machine. Synchronous inductance  $L_s$  stems from the inductance of the windings and encompasses the air gap inductance, slot leakage inductance, and end turn inductance. The back electromotive force  $E_f$  is generated through the flux linkage in the windings from the rotating magnetic field in the machine. Consequently,  $V_s$  denotes the stator terminal voltage.

$$E_f = k_{pm} \phi_m \omega_e \quad (23)$$

In this context:  $k_{pm}$  denotes the magnetic strength,  $\phi_m$  signifies the permanent magnet flux linkage, and  $\omega_e$  represents the electrical rotor angular speed. The expression for the back EMF can also be derived from Fig. 5 as follows:

$$E_f = k_{pm} \phi_m \frac{p}{2} \omega_m = V_s - i_s R_s - L_s \frac{di_s}{dt} \quad (24)$$

In this scenario, the connection between the electrical rotor speed ( $\omega_e$ ) and the mechanical rotor speed is expressed as follows:

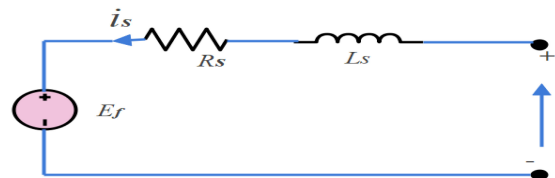


**Fig. 9.** Per phase model of WT-PMSG.

$$\omega_e = \frac{p}{2} \omega_m \quad (25)$$

The expression for the terminal stator voltage ( $V_s$ ) of the WT-PMSG can be articulated as follows:

$$V_s = i_s R_s + L_s \frac{di_s}{dt} + k_{pm} \phi_m \frac{p}{2} \omega_m \quad (26)$$

The rate of alteration of the complete flux linkage with each stator winding  $\phi_s$  is presented as given below:

$$\phi_s = \frac{d\phi_s}{dt} = L_s \frac{di_s}{dt} + k_{pm} \phi_m \frac{p}{2} \omega_m \quad (27)$$

By inserting (26) into (27), the ultimate expression for the terminal voltage ( $V_s$ ) of the PMSG can be written as:

$$V_s = i_s R_s + \frac{d\phi_s}{dt} \quad (28)$$

### VIII. MODELING OF THE IEEE LV DISTRIBUTION NETWORK AS A TEST CASE

The IEEE European LVDN is a standardized test system extensively employed in research and analysis related to the integration of DERs. Fig. 10 illustrates the single-line diagram of the examined unbalanced LVDN. This diagram represents an IEEE European test system commonly utilized in DERs integration studies. The network has a radial topology, a typical feature of European LVDNs. The test network connects to the main grid via an 800 kVA LV transformer, reducing the voltage from 11 kV to 416 V, with a delta/grounded star configuration. The transformer windings have a resistance of 0.4% and a reactance of 4%. Within this LVDN, three-phase residential consumers are connected at various points.

The consumption profiles are based on anonymized real-world data from the GA West Municipal District, with each consumer randomly assigned a profile from these recorded measurements. These load profiles are sampled at 1-hour intervals. Fig. 11 presents the aggregated demand of 31 consumers over 2 days. The model in this study focuses solely on active power, disregarding reactive power. Consequently, the power flow analysis assumes a constant power

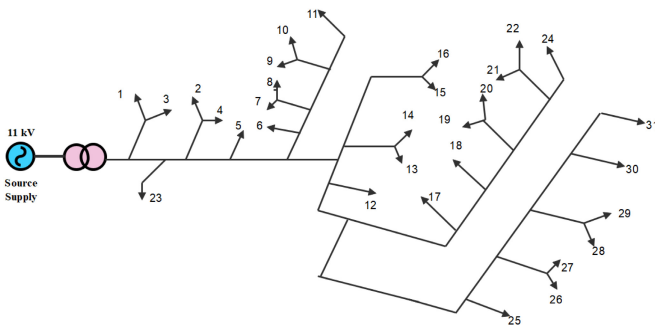


Fig. 10. Modified IEEE low-voltage distribution network (IEEE-LVDN).

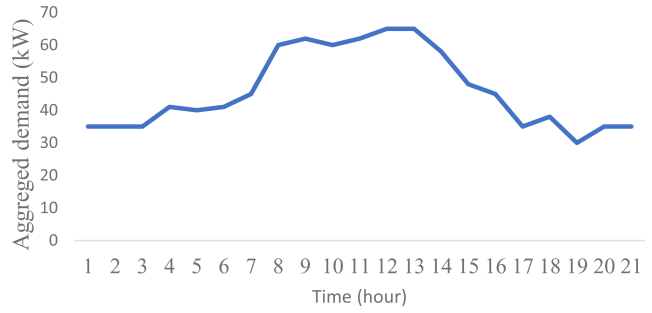


Fig. 11. Aggregated demand profiles of 31 homes.

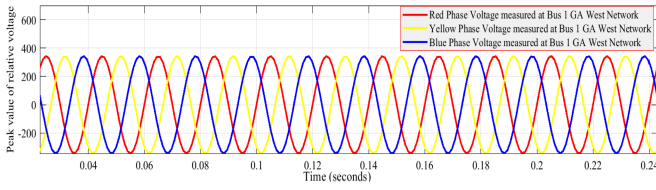
factor of 0.99 pu. Various legal and functional entities, such as the Energy Commission and the Electricity Company of Ghana, are being established to support this transition.

### IX. FINDING RESULTS

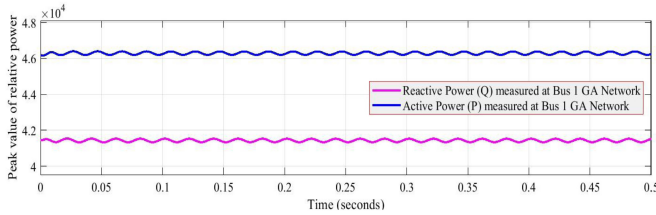
The results were obtained from the MATLAB/Simulink model of the GA West Network with voltage, current, active and reactive

TABLE III.  
POWER LOAD FLOW FOR GA NETWORK

Number of Bus	Active Power P (MW)	Reactive Power Q (MVAR)	Apparent Power (MVA)	PF
Bus 1	0.499997	0.5	0.7071	0.71
Bus 10	0.003662	-1.2E-17	0.00366	1
Bus 11	0.003662	-1.1E-17	0.00366	1
Bus 12	-8.7E-19	-9.7E-18	9.7-E-18	0.1
Bus 13	0.000732	-1E-17	0.00073	1
Bus 14	0.003662	-1.1E-17	0.00366	1
Bus 15	0.003662	-1.1E-17	0.00366	1
Bus 16	0.003662	-1.1E-17	0.00366	1
Bus 17	0.002441	-1.1E-17	2441	1
Bus 18	0.003662	-1.2E-17	0.00366	1
Bus 1	0.002441	-1.1E-17	0.00244	1
Bus 2	0.499992	0.499995	0.7071	0.71
Bus 3	0.003688	1.51E-13	0.00368	1
Bus 4	0.000244	-1.1E-17	0.00024	1
Bus 5	0.000488	-1.1E-17	0.00048	1
Bus 6	0.003688	2.84E-13	0.00368	1
Bus 7	0.003662	-1.1E-17	0.00366	1
Bus 8	0.001247	-1E-17	0.00124	1
Bus 9	0.003662	-1.2E-17	0.00366	1
<b>Total</b>	<b>1.044256</b>	<b>0.999995</b>	<b>1.04458</b>	<b>0.72</b>



**Fig. 12.** Peak value of relative voltage obtained at Bus\_1 GA West Network.



**Fig. 13.** Peak value of relative of power generated at Bus\_1 GA Network.

power, and power factor assessment of voltage levels at different node busbars. The voltage, current, and power factor assessment are compared. The model was modified to reflect the parameters of LV distribution grid components, as shown in Table III. Three-phase voltages and currents at different points in the system are compared by superimposing the simulation results. It is observed in Figs. 12–16 that the voltage level has improved compared to the voltage level across Bus (Fig. 10). It was observed that when the peak values of relative voltage, current, active, and reactive power were at Bus\_1, the overall current, voltage profile, and relative power generated by the system at Bus nos. 1, 2, 3, and 6 (Table III). The voltages remain within acceptable limits as defined by regulatory standards. Fig. 13 shows that the active and reactive power dissipated at Bus\_1 is higher than the relative power generated at Bus\_1, which could affect the quality of the power supply to connected loads. The current flow through various components, such as the transformer and distribution feeders, was observed. The assessment of reactive power flow, which indicates the exchange of reactive energy between components, can also affect voltage stability.

**X. RESULTS FOR GA WEST NETWORK CONNECTED WITH A FACTS DEVICE**

In the results for modeling GA networks with FACTS devices, from Figs. 17 to 19, it is observed that the voltage profile of the system

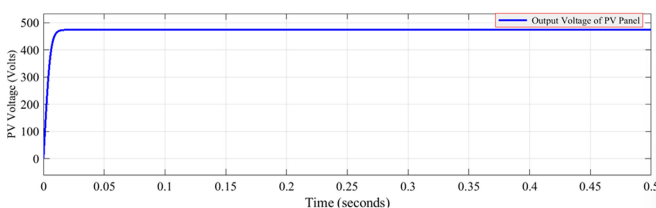


**Fig. 14.** Output voltage of PV panel.

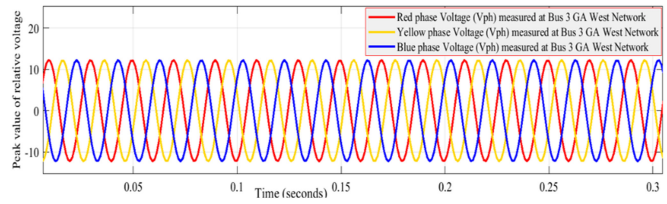


**Fig. 15.** Peak value of relative voltage obtained at Bus 3 GA-West Network.

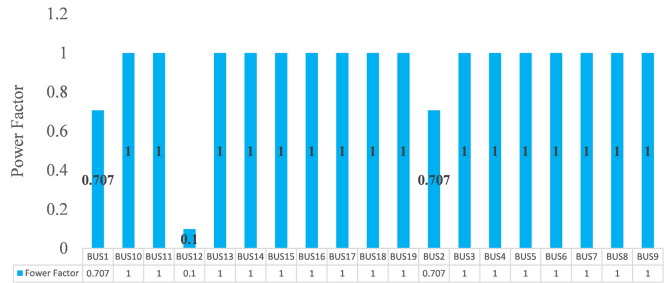


**Fig. 16.** Power factor generated when using GA network.

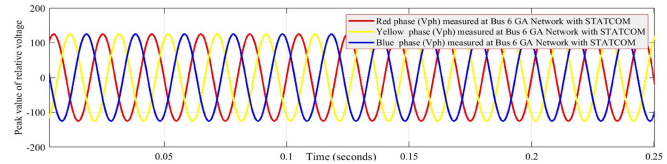


**Fig. 17.** Peak voltage obtained at Bus 6 when GA Network with STATCOM.

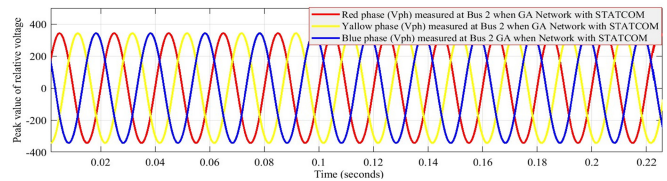


**Fig. 18.** Peak value of relative voltage obtained at Bus 2 when GA Network with STATCOM.

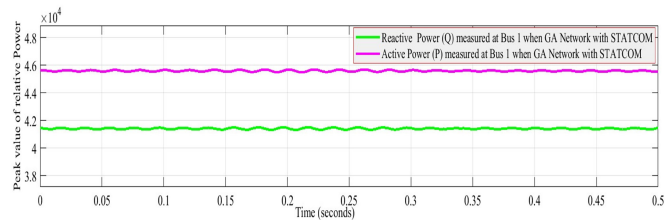


**Fig. 19.** Active power generated at GA Network Bus 1 with STATCOM.

improved after placement of the STATCOM. It was observed that the peak values of relative voltage, current, active, and reactive power at Bus\_1 using the GA Network with STATCOM all changed. The overall current, voltage profile, and relative power generated by the system improved at Bus nos. 1, 2, and 6 (Table IV). Without a STATCOM, the voltage profile across the network did not exhibit significant variations, especially under dynamic load changes. Voltage levels at various nodes deviated further from nominal values, potentially leading to voltage instability and sag/swell issues. Without a STATCOM, the network relied solely on traditional reactive power compensation devices, such as synchronous condensers. The reactive power exchange between nodes was less efficiently regulated, leading to larger reactive power flows and increased losses in the GA network. Without a STATCOM, power factor control was slitting less precisely, particularly under fluctuating load conditions. The GA network was experiencing low power factor performance, leading to increased losses and reduced efficiency in power distribution. Voltage stability and transient response were more susceptible to disturbances without the dynamic voltage support provided by the STATCOM.

**TABLE IV.**  
LOAD FLOW GA NETWORK WITH STATCOM

Number of Bus	Active Power P (MW)	Reactive Power Q (MVAR)	Apparent S (MVA)	Power Factor PF = P/S
Bus 1	0.02	0.02	0.028	0.71
Bus 10	0.002441	0.001221	0.002729	0.9
Bus 11	0.003662	-9.8E-18	0.003662	1
Bus 12	-1.4E-17	-1.8E-16	1.81E-16	0.08
Bus 13	0.003663	-1.1E-17	0.003662	1
Bus 14	0.003663	-1.1E-17	0.003663	1
Bus 15	0.003663	-1E-17	0.003662	1
Bus 16	0.003662	-1.2E-17	0.003662	1
Bus 17	0.002441	0.001221	0.002729	0.9
Bus 18	0.003662	-1E-17	0.003662	1
Bus 19	0.002441	-1.1E-17	0.002441	1
Bus 2	0.02	0.02	0.028	0.71
Bus 3	0.001243	0.000746	0.00145	0.85
Bus 4	0.002441	-1.1E-17	0.002441	1
Bus 5	0.000488	-1.1E-17	0.000488	1
Bus 6	0.003688	-3.9E-13	0.003688	1
Bus 7	0.003662	-1.1E-17	0.003662	1
Bus 8	9.17E-05	0.000114	0.000146	0.63
Bus 9	0.003668	-1.1E-17	0.003668	1
<b>Total</b>	<b>0.084582</b>	<b>0.043301</b>	<b>0.095</b>	<b>0.89</b>

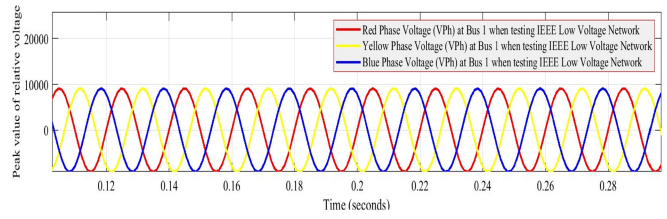


**Fig. 20.** Peak value of relative voltage at Bus\_1 using IEEE-LVDN.

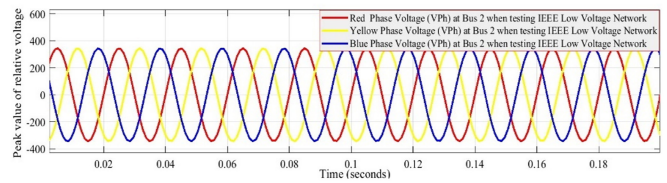


**Fig. 21.** Peak value of relative voltage at Bus\_2 using IEEE-LVDN.

**TABLE V.**  
LOAD FLOW WHEN TESTING IEEE-LVDN

Number of Bus	Active Power P (MW)	Reactive Power Q (MVAR)	Apparent S (MVA)	PF = P/S
Bus 1	0.001455	0.001455	0.00257	0.707
Bus 11	0.00375	-2.2E-15	0.00375	1
Bus 12	2.4E-15	-2.2E-15	3.26E-15	0.74
Bus 13	0.008125	-2.3E-15	0.008125	1
Bus 14	-3.8E-16	-2E-15	2.04E-15	0.2
Bus 15	0.006625	-2.3E-15	0.006625	1
Bus 16	0.002813	0.000125	2.82E-03	0.99
Bus 17	0.002188	-2E-15	0.002188	1
Bus 18	0.00475	-2.2E-15	4.75E-03	1
Bus 19	0.004063	-2.2E-15	0.004063	1
Bus 2	0.000145	0.000145	2.05E-04	0.707
Bus 20	0.002188	-2.2E-15	0.002188	1
Bus 3	0.0047	-2.4E-15	4.70E-03	1
Bus 3	0.002563	-2.2E-15	0.002566	1
Bus 4	0.004832	-2.2E-15	4.83E-03	1
Bus 5	3.16E-15	-7.1E-15	7.68 E-15	0.4
Bus 6	0.002554	0.000128	2.56E-03	0.99
Bus 7	2.41E-15	-2.1E-15	3.19E-15	0.75
Bus 9	0.005938	-2E-15	5.94E-03	1
Bus 10	0.007625	-2.2E-15	7.63E-03	1
<b>Total</b>	<b>0.064312</b>	<b>0.001853</b>	<b>6.43E-02</b>	<b>1</b>

**TABLE VI.**  
 COMPARISON OF ALL THE MODEL'S POWER FACTOR

Number of Bus	Model of IEEE-LVDN	Model GA Network	Model of GA Network with FACTS Device	Model of Hybrid Connected to GA Network
Bus 1	0.707	0.707	0.707	5.00E-05
Bus 10	1	1	0.9	4.00E-07
Bus 11	0.74	1	1	1
Bus 12	1	0.1	0.4	1
Bus 13	0.2	1	0.07	1
Bus 14	1	1	1	1
Bus 15	0.99	1	1	1
Bus 16	1	1	1	1
Bus 17	1	1	0.9	4.00E-07
Bus 18	1	1	1	1
Bus 19	0.707	1	1	1
Bus 2	1	0.71	0.707	5.00E-05
Bus 3	1	1	0.85	3.40E-05
Bus 4	1	1	1	1
Bus 5	1	1	1	1
Bus 6	0.4	1	1	1
Bus 7	0.99	1	1	1
Bus 8	0.75	1	0.63	1
Bus 9	1	1	1	1

Transient voltage graphs or spikes occurred more frequently, potentially affecting sensitive loads and equipment. Without dynamically injecting or absorbing reactive power, load balancing across phases and node busbars was less effective. Some loads experienced higher voltage variations or voltage imbalances, affecting their performance and reliability.

**XI. RESULTS FOR MODELING TEST SYSTEM: MODIFIED IEEE DISTRIBUTION NETWORK**

The results from Figs. 17 to 21 and Tables IV show that the voltage profiles of the IEEE LV distribution system have improved. Figs. 18

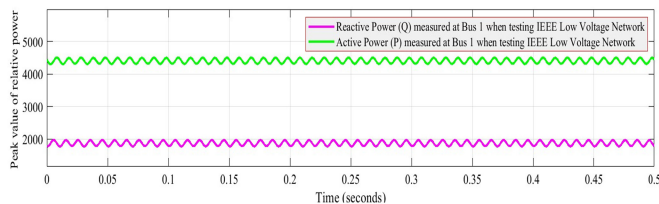


**Fig. 22.** Peak value of relative power measured at Bus\_1 using IEEE-LVDN.

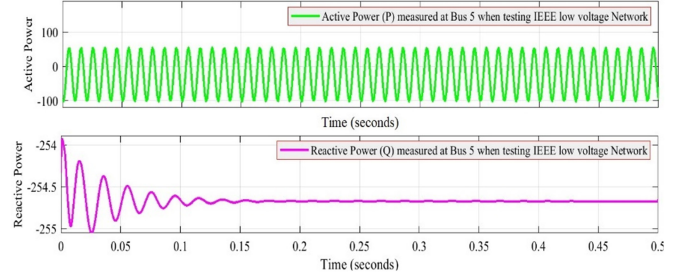


**Fig. 23.** Peak value of relative power measured at Bus\_5 using IEEE-LVDN.

and 19 show the various power generated at Bus nos. 1, 2, and 3. The load flow findings from the power load flows and power factors of the benchmark IEEE-LVDN are compared to validate the model.

**XII. VALIDATION OF GA-WEST NETWORK AND MODIFIED IEEE**

The comparison reveals that both networks perform well in power factor management, with the modified IEEE-LVDN showing slightly better power factor values under all conditions. However, both networks experience a drop in power factor during peak load conditions, which is expected due to the increased reactive power demand. The sensitivity analysis highlights the importance of effective power factor correction devices to maintain high power factor values. By following this detailed validation process, it is observed from Table VI that the power factor performance of the GA-West Network has more unity power factor than modified IEEE-LVDN. They accurately assessed and compared, leading to insights for further improvement and optimization. From the comparison of the peak levels of relative current, voltage, and power generated in Tables VI and Fig. 17-15, especially Fig. 25 it is observed that the voltage profile and power of the system have improved. The overall active power generated by the system has improved when testing with IEEE-LVDN at Bus nos. 1, 2, 3, and 4, respectively.

From the comparison in Fig. 25, it is observed that the real power loss of the system has been reduced after the placement of STATCOM. The overall real power loss of the system has decreased with the increase in the size of the FACTS device, and the majority of buses measured approach a power factor of 1 (Table IV). When analyzing the overall performance from the tables and the graphs, it is observed that the various reactive power values are minimal when the system is connected to the FACTS device. It was observed that the reactive power loss of the system has been reduced after the placement of the FACTS device. The overall reactive power loss of the system has decreased with an increase in size as compared to STATCOM, and after that, reactive power loss increased again and has a higher absorption power. Fig. 17 and Table IV detail the power factor on each line, as well as the power factor on each line. The addition of FACTS devices to Bus 3 increased both active power loss and reactive power loss for many lines in the system. The power factor comparison indicated that the system with the FACTS device had a higher power factor, closely approaching that of the other device. A power factor close to 1 is desirable for minimizing losses in the system.

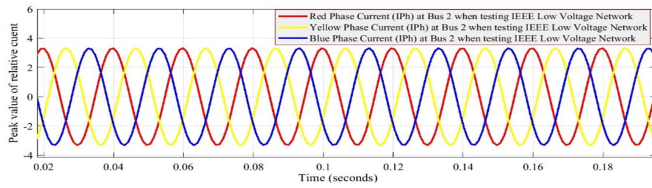


Fig. 24. Peak value of relative current at Bus\_2 using IEEE-LVDN.

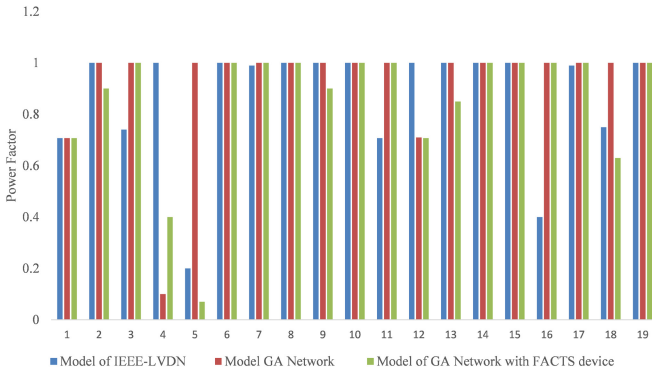


Fig. 25. Comparison of power factor.

Validating the GA-West Network and the modified IEEE-LVDN for load flow analysis involves the accuracy and reliability of the simulation model. Load flow analysis is crucial for understanding the steady-state operation of electrical power systems, including voltage profiles, power losses, and the loading of network components. The validation ensures that the performance of load flow and power factor calculations at various buses for the GA-West Network and the modified IEEE-LVDN are accurate, reliable, and reflective, as observed from Fig. 15 and the corresponding graphs. The comparison between the GA-West Network and the modified IEEE-LVDN reveals that the GA-West Network demonstrates slightly improved energy efficiency. Additionally, significant enhancements were observed in key values. However, the IEEE-LVDN achieved a power factor closer to unity, effectively reducing power losses within the power system network.

### XIII. CONCLUSION

This study investigates the impact of FACTS devices on power factor in LV networks connected to renewable energy sources, specifically PV solar and wind turbines, within the GA West Municipal District electricity grid in Accra, Ghana. As renewable energy use grows, understanding its effect on LV networks and optimizing management strategies is crucial. The research models and simulates the GA-West Network and the IEEE-LVDN to assess the performance of FACTS devices, specifically the STATCOM, with a focus on power factor, active, and reactive power. A 19-busbar test network was modeled to evaluate the integration of PV and wind turbine systems, with IEEE-LVDN used for validation. MATLAB/Simulink simulations reveal that FACTS devices significantly improve the power factor, achieve near-unity levels, reduce active and reactive power losses, and enhance overall network performance. Instead, active

and reactive powers were 293.8 MW and  $-43.5$  MVA, with a power factor of 0.99 at Bus 2. Systems with FACTS devices showed better performance in active and reactive power and power factors. These findings demonstrate that FACTS devices play a key role in managing power quality and optimizing the performance of renewable energy systems in grid-connected networks. This study concluded that:

- There was an improvement in power factor when the FACTS device was installed in the system network approximately to 1.
- There was a significant enhancement in values. The power factor of the IEEE-LVDN bus system has been improved to a more unity power factor.
- Inject active and reactive power flow in the power system network, active power loss and reactive power loss are minimized.

**Peer-review:** Externally peer-reviewed.

**Availability of Data and Materials:** The data that support the findings of this study are available on request from the corresponding author.

**Author Contributions:** Concept – J.A.; Design – J.A.; Supervision – P.A., F.S.; Resources – J.A.; Materials – J.A.; Data Collection and/or Processing – J.A.; Analysis and/or Interpretation – J.A., A.A.; Literature Search – J.A.; Writing – J.A.; Critical Review – J.A.

**Acknowledgments:** This work was performed at the Akenten Appiah-Menka University of Skills Training and Entrepreneurial Development (AAMUSTED), Power and Energy Research Laboratory (PERL). The authors appreciate the use of PERL facilities and resources.

**Declaration of Interests:** The authors have no conflicts of interest to declare.

**Funding:** This study received no funding.

### REFERENCES

1. P. Sivaraman, and C. Sharmeela, "Power system harmonics," *Power Qual. Mod. Power Syst.*, pp. 61–103, 2020. [\[CrossRef\]](#)
2. R. O. Olarewaju, A. S. O. Ogunjuyigbe, T. R. Ayodele, A. A. Yusuff, and T. C. Mosetlhe, "An assessment of proposed grid integrated solar photovoltaic in different locations of Nigeria: Technical and economic perspective," *Clean Eng. Technol.*, vol. 4, p. 100149, 2021. [\[CrossRef\]](#)
3. O. Bamisile, Q. Huang, P. N. Ayambire, and P. Anane, "Analysis of Solar PV and Wind Power Penetration into Nigeria Electricity System,' no," August, pp. 6–11, 2020. [\[CrossRef\]](#)
4. M. Jafar, and H. Moghaddam, *Power Quality Improvement in the Distribution Network Using Optimization of the Hybrid Distributed Generation System*, 2021.
5. A. I. Nousedlis, A. I. Chrysochos, G. K. Papagiannis, and G. C. Christoforidis, "The impact of Photovoltaic Self-Consumption Rate on voltage levels in LV distribution grids," in *Inst. Electr. Electron. Eng. Inc.*, 11th IEEE International Conference on Compatibility, Power Electronics and Power Engineering, CPE-POWERENG 2017, 2017, pp. 650–655. [\[CrossRef\]](#)
6. M. Nour, J. P. Chaves-Avila, M. Troncia, A. Ali, and Á. Sanchez-Miralles, "Impacts of community energy trading on low voltage distribution networks," *IEEE Access*, vol. 11, pp. 50412–50430, 2023. [\[CrossRef\]](#)
7. A. Benali, M. Khat, T. Allaoui, and M. Denai, "Power quality improvement and low voltage ride through capability in hybrid wind-PV farms

- grid-connected using dynamic voltage restorer," *IEEE Access*, vol. 6, pp. 68634–68648, 2018. [\[CrossRef\]](#)
8. I. B. Majeed, and N. I. Nwulu, "Impact of reverse power flow on distributed transformers in a solar-photovoltaic-integrated low-voltage network," *Energies*, vol. 15, no. 23, 2022. [\[CrossRef\]](#)
  9. J. Abban, and A. Awopone, "Techno-economic and environmental analysis of energy scenarios in Ghana," *Smart Grid Renew. Energy*, vol. 12, no. 6, pp. 81–98, 2021. [\[CrossRef\]](#)
  10. O. Gandhi, D. S. Sampath, C. D. Rodríguez-Gallegos, and D. Srinivasan, "Review of power system impacts at high PV penetration Part I: Factors limiting PV penetration," *Sol. Energy*, vol. 210, no. February, pp. 181–201, 2020. [\[CrossRef\]](#)
  11. A. A. Shehata, M. A. Tolba, A. M. El-Rifaie, and N. V. Korovkin, "Power system operation enhancement using a new hybrid methodology for optimal allocation of FACTS devices," *Energy Rep.*, vol. 8, pp. 217–238, 2022. [\[CrossRef\]](#)
  12. Y. Kebbati, and L. Baghli, "Design, modeling and control of a hybrid grid-connected photovoltaic-wind system for the region of Adrar, Algeria," *Int. J. Environ. Sci. Technol. (Tehran)*, vol. 20, no. 6, 6531–6558, 2023. [\[CrossRef\]](#)
  13. N. H. Baharudin et al., "Design and Performance Analysis of Grid Connected Photovoltaic (GCPV) based DSTATCOM for Power Quality Improvements," *J. Phys.: Conf. Ser.*, vol. 1878, no. 1, 2021. [\[CrossRef\]](#)
  14. M. Abdullah, L. Hassan, M. Moghavvemi, M. K. Abdullah, and L. H. Hassan, "Voltage stability assessment of grid connected PV systems with FACTS devices," 2021. [\[CrossRef\]](#)
  15. M. Yaseen et al., *A Review of Supercapacitors: Materials Design, Modification, and Applications*. MDPI, 2021. [\[CrossRef\]](#)
  16. A. Sabo, B. Y. Kolapo, T. E. Odoh, M. Dyari, N. I. A. Wahab, and V. Veerasamy, *Solar, Wind and Their Hybridization Integration for Multi-machine Power System Oscillation Controllers Optimization: A Review*. MDPI, 2023. [\[CrossRef\]](#)
  17. K. K. Kumar, T. K. Kumar, and N. Siddhik, "Power quality improvements in grid-connected PV system using novel optimization technique," *Int. J. Recent Technol. Eng.*, vol. 8, no. 3, pp. 6104–5110, 2019. [\[CrossRef\]](#)
  18. R. Sadiq, Z. Wang, C. Y. Chung, C. Zhou, and C. Wang, "A review of STATCOM control for stability enhancement of power systems with wind/PV penetration: Existing research and future scope," *Int. Trans. Electr. Energ. Syst.*, vol. 31, no. 11, 2021. [\[CrossRef\]](#)
  19. H. D. Tafti et al., "Extended functionalities of photovoltaic systems with flexible Power Point tracking: Recent advances," *IEEE Trans. Power Electron.*, vol. 35, no. 9, pp. 9342–9356, 2020. [\[CrossRef\]](#)